

Supporting Information

Cuboidal supraparticles self-assembled from cubic CsPbBr_3 perovskite nanocrystals

Julia S. van der Burgt^{1}, Jaco J. Geuchies^{1*}, Berend van der Meer², Hans Vanrompay³,
Daniele Zanaga³, Yang Zhang³, Wiebke Albrecht², Andrei V. Petukhov^{4,5}, Laura Filion², Sara
Bals³, Ingmar Swart¹, Daniël Vanmaekelbergh¹*

1. Condensed Matter and Interfaces, Debye Institute for Nanomaterials Science, Utrecht University
2. Soft Condensed Matter, Debye Institute for Nanomaterials Science, Utrecht University
3. Electron Microscopy for Materials Science, University of Antwerp
4. Physical and Colloidal Chemistry, Debye Institute for Nanomaterials Science, Utrecht University
5. Laboratory of Physical Chemistry, Department of Chemical Engineering and Chemistry, Eindhoven University of Technology

*These authors contributed equally

METHODS

Synthesis of CsPbBr₃ nanocrystals (NCs). The CsPbBr₃ NCs were prepared according to the method described by Protesescu *et al.*¹ First, Cs-oleate precursor stock solution was prepared. Cs₂CO₃ (0.814g, 99%, Aldrich), 2.5 mL OA (90%, Aldrich) and 40 mL ODE (90%, Aldrich) were loaded into a 100 mL round-bottom flask. The mixture was dried under vacuum for approximately 1h at 120 °C, and then heated under N₂ to 150 °C until all Cs₂CO₃ had reacted with OA. ODE (5 mL) and PbBr₂ (0.069g, 99.999%, Aldrich) were loaded into a separate 25 mL flask and dried under vacuum for 1h at 120 °C. OLAM (0.5 mL, 70%, Aldrich) and OA (0.5 mL) were injected at 120 °C under N₂ atmosphere. After PbBr₂ had dissolved, the temperature was raised to 180 °C and a 0.4 mL portion of the Cs-oleate stock solution was quickly injected. We note that the Cs-oleate stock solution had to be preheated to ~100 °C before injection. After five to ten seconds the reaction mixture was cooled by an ice-water bath in order to quench the reaction. The size of the nanocubes was determined as described in Figure S1.

Purification of the nanocrystals. The CsPbBr₃ NCs were purified following the method described by De Roo *et al.*⁶¹ (for a synthesis based on 69 mg of PbBr₂). The crude synthesis solution was centrifuged for 3 min at 10 000 rpm and the colored supernatant was discarded. Then, 300 µL of hexane was added and the NCs were dispersed using a vortex mixer. Subsequently, the suspension was again centrifuged for 3 min at 10 000 rpm, after which the precipitate, containing larger NCs and agglomerates, was discarded. Another 300 µL of hexane was added to the supernatant, resulting in a colloidal dispersion of CsPbBr₃ NCs.

Self-assembly of the NC solutions into supraparticles. The CsPbBr₃ NCs were self-assembled into cuboidal supraparticles by adding a varying amount of methyl acetate into a solution containing 0.1 µM NCs (as determined with absorption spectroscopy¹). The samples were incubated at room temperature in a dark storage area for five days, unless mentioned otherwise. Self-assembly through solvent-evaporation occurred in NC solutions with a concentration higher than 1 µM NCs. Note that

the latter number is a rough estimate, since the exact determination of the concentration was hampered due to saturation of the absorption signal.

Transmission SAXS and WAXS experiments. Small and wide-angle X-ray scattering (SAXS and WAXS) experiments were performed at the ID02 beamline of the European Synchrotron Radiation Facility (ESRF), Grenoble, France. The SAXS detector was a Rayonix MC-170HS mounted at a distance of 1m from the sample inside a vacuum tube to background scattering from air. The WAXS detector was a Rayonic LX-170HS (calibrated with α -Al₂O₃), which was mounted at the beginning of the vacuum tube. The combination of detectors allowed us to measure a q-range of 6.5×10^{-2} nm⁻¹ to 4.8 nm⁻¹. The wavelength of the collimated X-ray beam was 0.1 nm (12.4 keV). A quartz capillary (with an inner diameter of 1 mm and 10 μ m wall thickness) with a NC solution in toluene (or a diluted solution of NCs in toluene with methyl acetate) was placed inside a Linkam stage.

Optical spectroscopy. Samples for optical measurements and time-resolved optical spectroscopy (TRES) were prepared by diluting the colloidal dispersion of NCs with anhydrous toluene under nitrogen and stored in sealed quartz cuvettes. Absorption spectra were measured on a double beam Perkin-Elmer Lambda 16 UV/Vis spectrometer. Photoluminescence (PL) spectra were recorded on an Edinburgh Instruments FLS920 Spectrofluorimeter equipped with a 450 W Xenon lamp as excitation source and double grating monochromators. PL decay curves were obtained by time-correlated single-photon counting on a Hamamatsu H7422-02 photomultiplier tube with low dark count rate (< 10 cts/s). A pulsed diode laser (EPL-445 Edinburgh Instruments, 375 nm, 55 ps pulse width, 0.2 MHz repetition rate) was used as the excitation source.

Confocal microspectroscopy. Individual supraparticles were studied using a Leica TCS SP8 confocal microscope. We used a 63x/1.4 oil-immersion confocal Leica objective. The sample was excited with a fiber-based white light laser at 470 nm. A droplet of the dispersion containing supraparticles was placed on a microscope slide and the solvent (toluene) was allowed to evaporate. A droplet of immersion oil was placed on top of the sample to index-match the oil objective, followed by another

cover microscope slide (with a thickness of 160-190 μm). Another droplet of immersion oil was placed on top of the cover slide before placing the sample into the microscope.

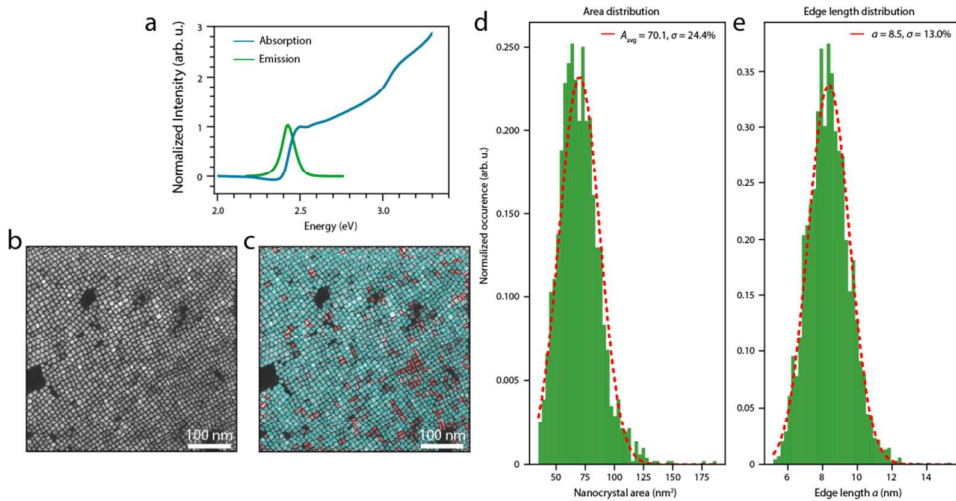


Figure S1: Characterization of the as-synthesized CsPbBr_3 perovskite NCs. (a) Normalized optical absorption (blue) and PL (green) spectra of the as-synthesized nanocubes in toluene. (b) HAADF-STEM image of a sub-monolayer of the NCs. (c) Computer aided image analysis allows us to obtain statistics on the size and shape of the particles. Particles with an aspect ratio ≤ 1.5 are defined as cubic and are outlined with a blue square. Particles with an aspect ratio > 1.5 are defined as platelet-like and are outlined with a red rectangle. (d) Distribution of the areas of the detected NCs. (e) Distribution of the detected edge-lengths of the NCs. Several HAADF-STEM micrographs were used to gather statistics of over 5000 NCs.

We characterized the optical absorption and emission spectra in solution (toluene). Throughout the article we used several different batches of NCs, all showing emission around 2.4 eV with a narrow FWHM (<80 meV). The PL quantum yield varies in between batches in between 85% and 95% as determined with an integrating sphere. Figure S1(a) shows the characteristic absorption and emission spectra for the NCs with an edge length of roughly 8.5 nm. The NCs are in the weak confinement regime (Bohr exciton radius of 3.5 nm) and no clear bulk excitonic peak is visible in the absorption spectrum.

The geometry of the NCs was characterized by high-angle annular dark-field (HAADF) scanning transmission electron microscopy (STEM). We employ a custom made Python code to gather information on the geometry of the synthesized NCs. The process is schematically outlined in Figure S2. After filtering and binarizing the image, the particles are fitted with a rectangle. The results of the particle detection are shown in Figure S1(c). We define particles with an aspect ratio 1.5 as cubic and outline the detected shape with a blue square. Detected particles with an aspect ratio > 1.5 are defined as rectangular, and are

outlined with a red rectangle. Over 95% of the particles in a single HAADF-STEM image are detected, and the resulting outlines seem to match the particle contours very well. Over 5000 particles were analyzed over several HAADF-STEM images, which allowed us to obtain decent statistics on the particle size and shape. The area of the detected particles is shown in Figure S1(d) and the detected nanocube edge-length is shown in Figure S1(e). The acquired data is binned into a histogram and fitted with a normal distribution. The nanocrystals have {100} facets with an average surface area of $70 \pm 17 \text{ nm}^2$ and an edge length of $8.5 \pm 1.1 \text{ nm}$.

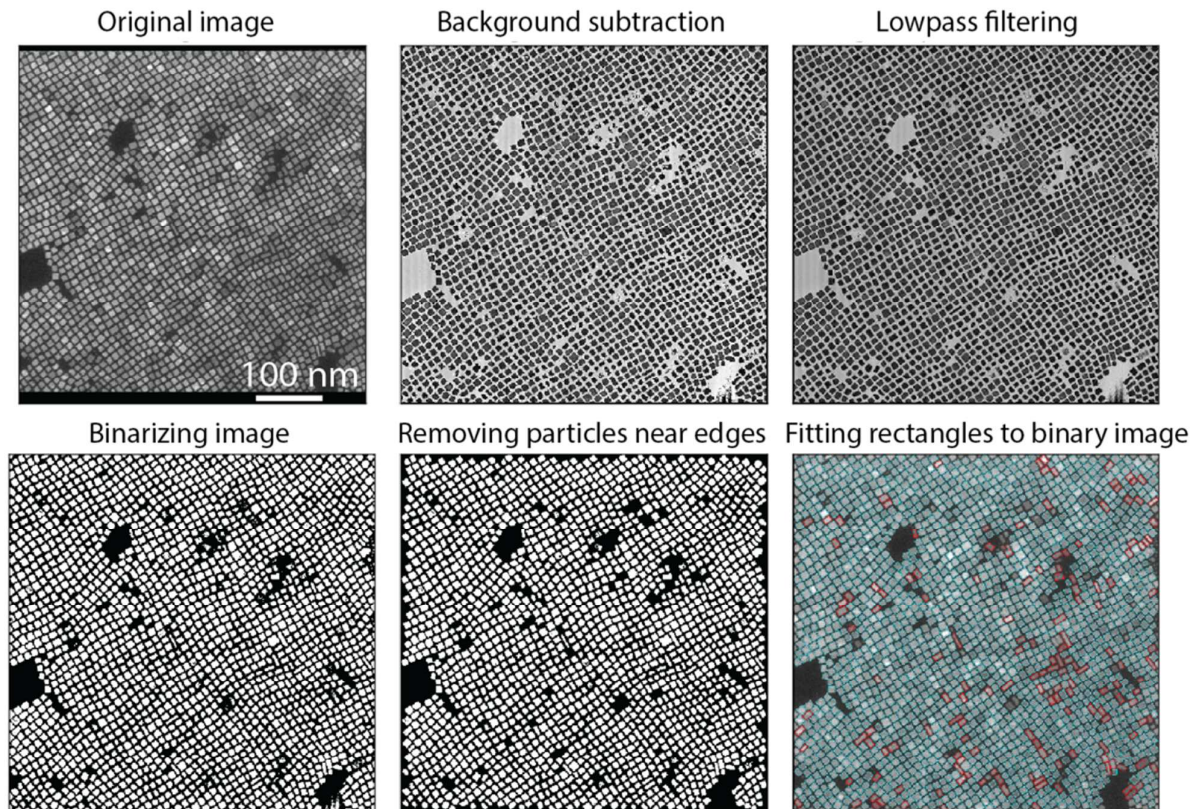


Figure S2: Schematic outline of the used particle detection scheme. An electron micrograph is loaded into the program. The background is detected by fitting each column of the image matrix with a third-order polynomial and this is subtracted from the original. After this the image is low-pass filtered through a Fast-Fourier Transform. The resulting filtered image is binarized and particles near the edges are filtered out, before fitting the binary areas with rectangles. The particles are defined cubic and labeled blue for aspect ratio's ≤ 1.5 . Particles with an aspect ratio > 1.5 are defined as platelet-like and are labeled red.

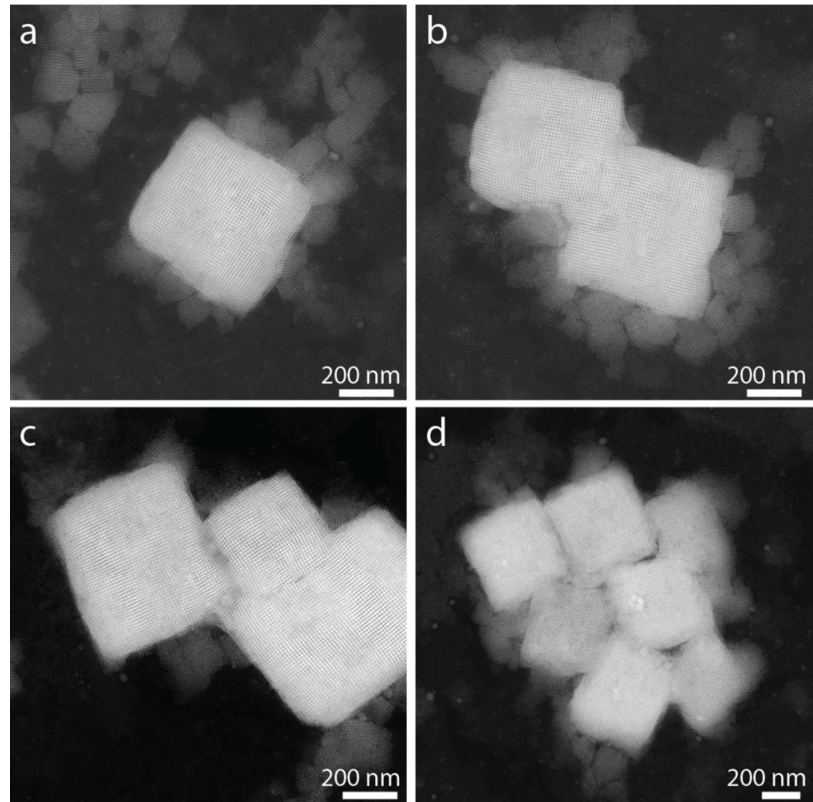


Figure S3: HAADF-STEM overview images of typically encountered supraparticles. (a) Single supraparticles are most commonly observed. (b) Micrograph of two aggregated supraparticles. (c) Micrograph of three aggregated supraparticles. (d) Micrograph of multiple aggregated supraparticles. Note how (b) and (c) appear the same orientation of the NC lattice, whereas in (d) the rotational disorder is larger.

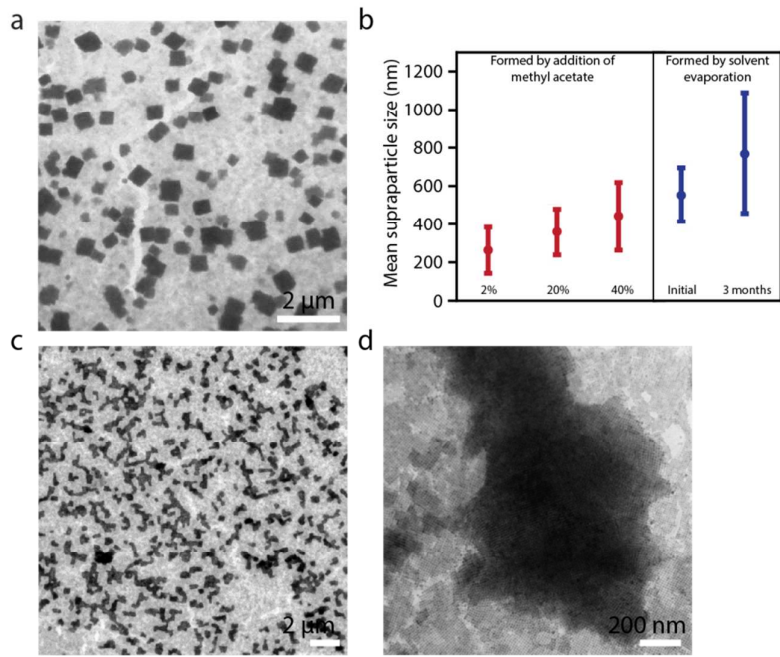


Figure S4: Supraparticle growth over time. **(a)** Bright-field TEM overview image of supraparticles, grown by addition of methyl acetate up to a volume fraction of 0.2. The TEM image was taken one week after addition of methyl acetate. **(b)** Average supraparticle size after one week of growth (for anti-solvent addition), and by solvent evaporation after one month and after three months. The error bars depict the standard deviation of the size dispersion. **(c)** Upon increasing the volume fraction of methyl acetate above 0.4 (here 0.5), the supraparticles possess irregular shapes and **(d)** the NCs appear randomly agglomerated.

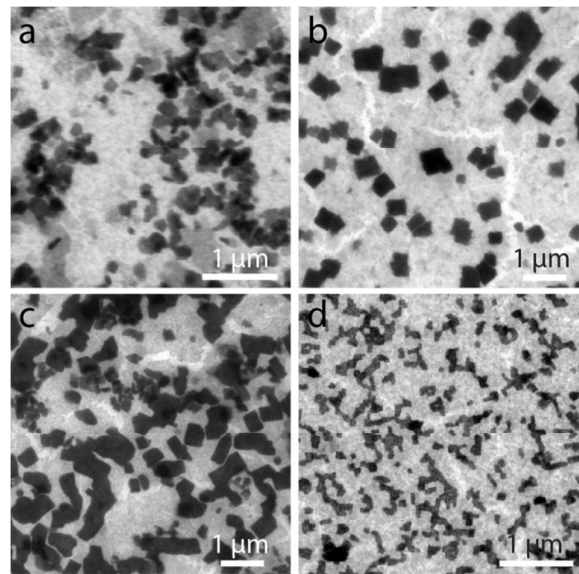


Figure S5: Effect of the amount of added anti-solvent on the supraparticle formation.
From **(a)** to **(d)** we have added a volume fraction of 8%, 20%, 40% and 80% methyl acetate to the NC dispersion respectively. There is still NC order visible in the sample displayed in **(c)**, but the supraparticle outline show less sharp edges. In **(d)** there is no NC order inside the agglomerates.

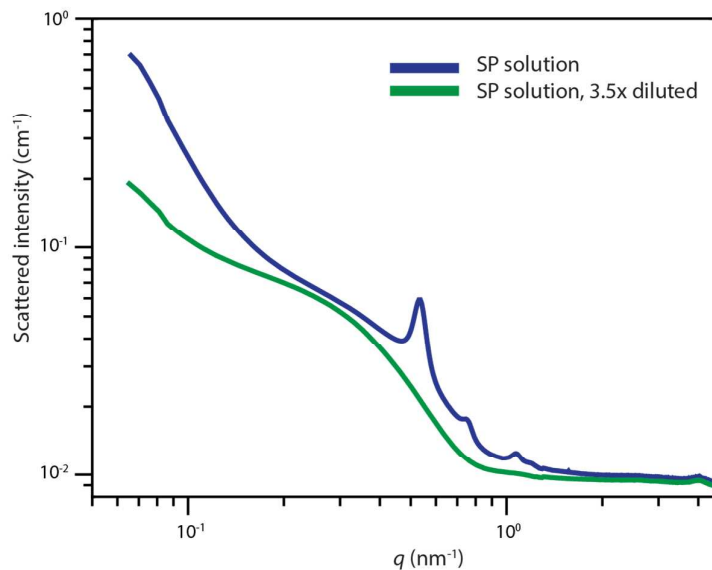


Figure S6: Transmission SAXS, showing the dissolution of the supraparticles. The solution of supraparticles in toluene (blue curve) is 3.5 times diluted with additional toluene (green curve). As can be observed, the structure factor peaks, originating from the supraparticles, disappear and only form factor scattering of the NCs in solution is observed; the supraparticles redissolve upon dilution.

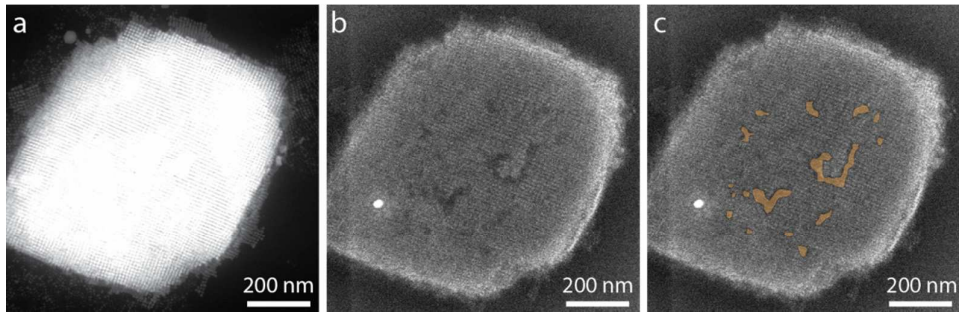


Figure S7: SE-STEM imaging of the surface of a supraparticle. (a) HAADF-STEM image of a supraparticle. (b) Corresponding SE-STEM image of the supraparticle. The missing NCs appear as darker grey area on the surface of the supraparticle. The white spot is a result of carbon build up by the electron beam. (c) For clarity, the regions with missing NCs are indicated in yellow. From all obtained SE-STEM images we estimate that the total amount of missing surface NCs equals $5.5 \pm 1.5\%$ of the total surface area of the supraparticle.

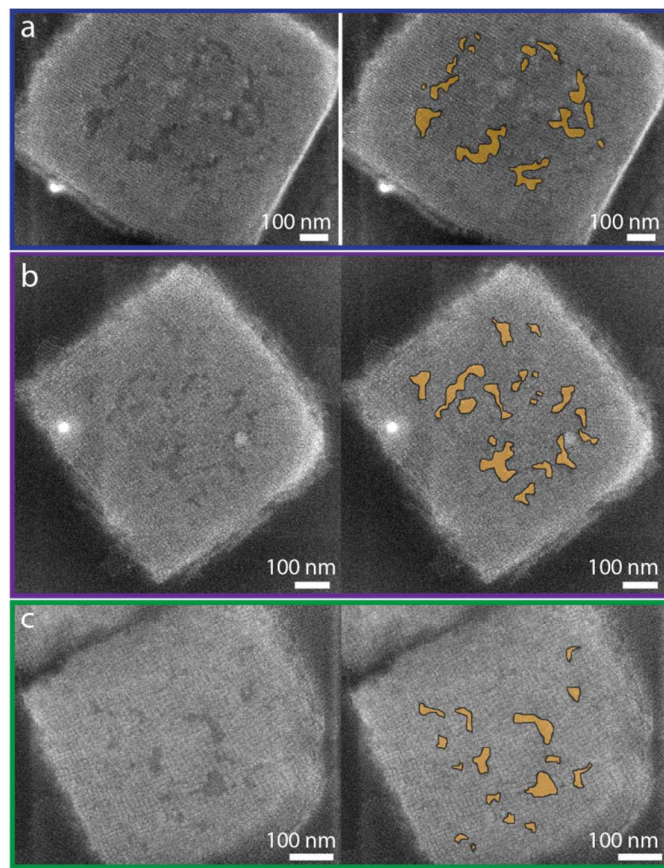


Figure S8: SE-STEM micrographs of more supraparticles, showing the presence of localized surface defects. (a-c) Images of several supraparticles, all of which contain surface defects in the form of missing (groups of) NCs. The area's containing the defects appear as slightly darker gray and are highlighted in yellow in the right column of images. We manually estimated the area of the surface defects.

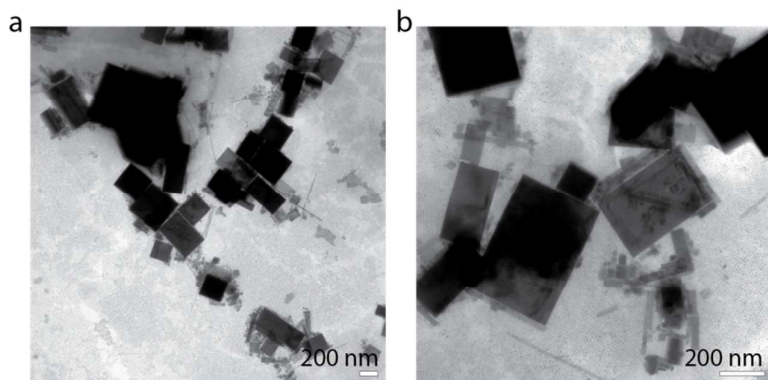


Figure S9: Formation of single crystalline particles from SPs. (a) and (b) both show bright-field TEM images of a sample which was left to incubate for two weeks in a solution with a volume fraction of 20% methyl acetate. The SPs which were observed in dispersion a week earlier seem to have transformed into single crystalline sheets of CsPbBr₃. Possibly the ligands are slowly removed from in between the NCs inside the dispersion containing the anti-solvent, allowing the NCs to fuse epitaxially. However, this remains to be verified experimentally.

High-angle annular dark-field scanning transmission electron microscopy (HAADF-STEM) tomography

The nanocube assembly was investigated using HAADF-STEM tomography. During a tomography experiment the three-dimensional object is retrieved from a set of two dimensional projection images. Only when the intensity in the measurement is a monotonic function of a property of the imaged object, they qualify as a projection². In HAADF-STEM, the image intensity scales with both the atomic number of the elements present in the sample as well as the thickness of the object, consequently fulfilling the stated requirement

Since a gap in angular range is often unavoidable due to the limited space between the pole pieces of the objective lens in the electron microscope or shadowing effects occurring at high tilt angles, this set of equations is often underdetermined, and no exact solution exists at all. Here, we will make use of the simultaneous iterative reconstruction algorithm (SIRT) in order to retrieve the 3D morphology in an iterative manner³.

A practical approach to reduce the influence of the missing wedge is to acquire a second orthogonal tilt and combine it with the former to reduce the missing wedge of information to a missing pyramid. The alignment of the tilt series was performed in the following manner. The first tilt series was aligned by using cross-correlation routines⁴. An intermediate reconstruction was then calculated and used to simulate projections along the directions where the second series was acquired. The projections of the second tilt series were then aligned through cross-correlation between the simulated and experimental projections. Using the dual tilt series as input for the SIRT algorithm we were able to enhance the quality of the tomographic reconstruction^{5,6}, as indicated by Figure S11.

We were able to visualize the nanocubes from several directions, the missing pyramid artefacts still hampered the full reconstruction of the nanocube positions. Yet, utilizing the prior information on the cubic periodicity, we can estimate the volume fraction of vacancies in the bulk of the supraparticle.

After Fourier filtering the reconstruction, the result was automatically segmented using Otsu thresholding (Figure S10 b)⁷. To determine the volume of NCs, the binarized volume was divided by the third order of the periodicity measured from a 2D intensity profile (Figure S10 b).

The volume of vacancies was found by inverting the segmented volume and removing unrealistically large connected components (Figure S10 c-d).

Combining the information from the above figure, we can conclude that:

- The assembly contains 5.529 nanocubes, accounting for a volume of 1.324.200 voxels.
- The empty space inside the superlattice equals 43894 voxels.
- The volume fraction of NC vacancies is hence roughly 3.31%.

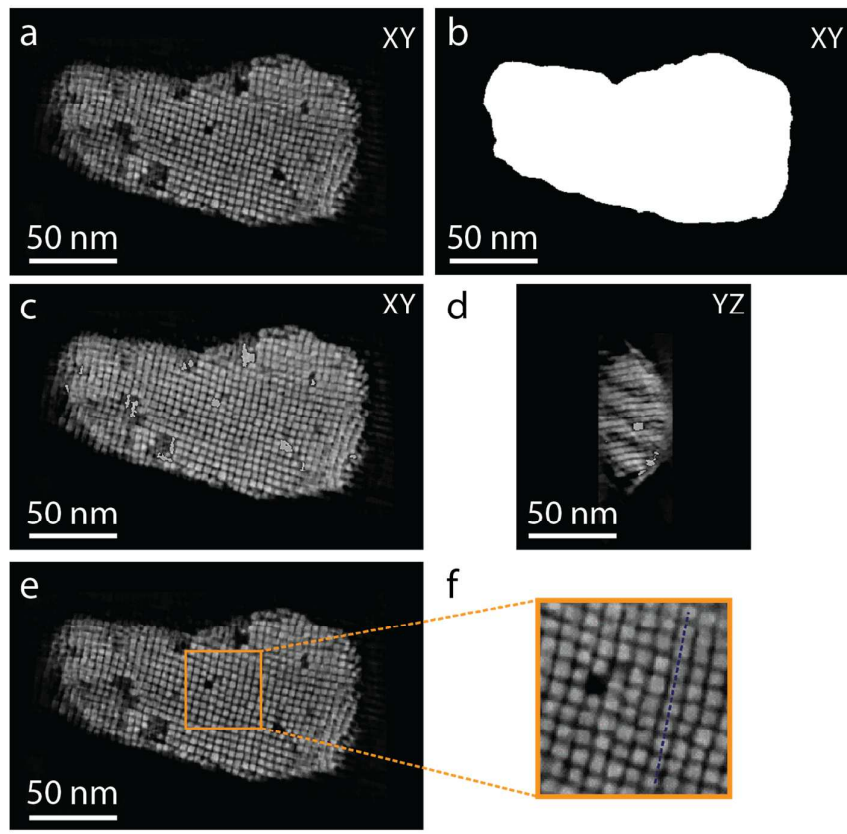


Figure S10: Determination of the volume fraction of defects in the bulk of a SP through HAADF-STEM tomography. The individual nanocubes are only well visible in the XY orthoslices (**a**) and not in the directions perpendicular to this plane. (**b**) Determination of the total volume of the SP by summing up the voxels of the segmented image. (**c-d**) Automatic segmentation of the void space inside the SP and determination of their volume. (**e**) To take into account that there exists space in between the different nanocubes, we determine the size of the cubes and the size of the gaps in between the particles by an intensity profile over the particles (**f**).

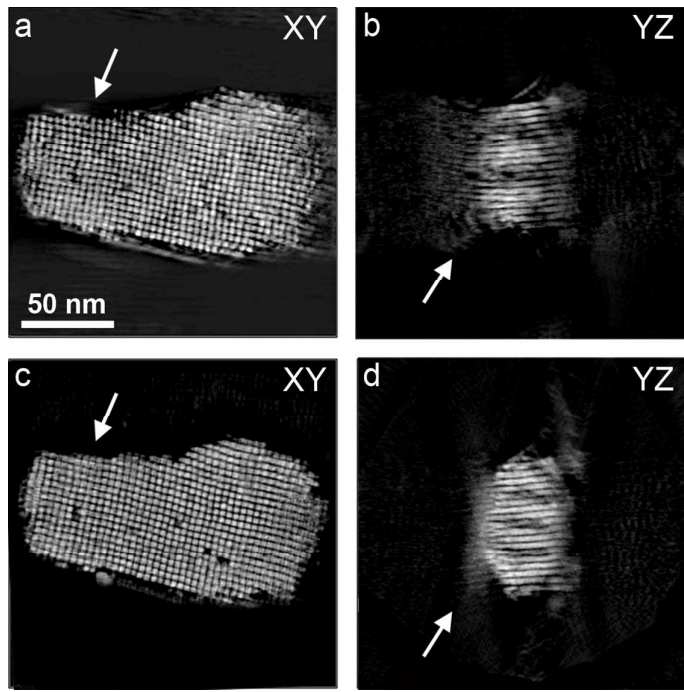


Figure S11: Quality assessment of dual tilt-axis tomography. A comparison is given between the central XY and YZ orthoslices through the SIRT reconstruction based on (**a-b**) single tilt-axis acquisition or (**c-d**) dual tilt-axis acquisition. As indicated by the white arrows, the dual tilt-axis reconstruction does not only improve the overall shape of the supraparticle in comparison to the single tilt-axis reconstruction, but it also results in a more refined reconstruction.

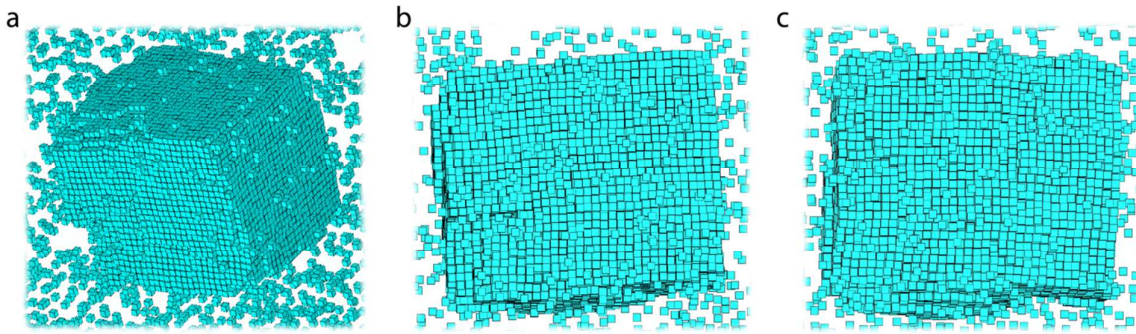


Figure S12: Monte Carlo simulations of the nucleation of the supraparticle for a system of parallel attractive cubes. (a) The nanocubes have nucleated into a ‘more or less’ cubic supraparticle. (b,c) Two different faces of the supraparticle, showing the cubic structure of the supraparticle.

We study the nucleation of a simple model system for our nanocubes. More specifically we perform Monte Carlo simulations of attractive cubes in the NVT ensemble, where N (the number of cubes), V (the volume) and T (the temperature) are fixed. The interactions between the cubes are modelled as a combination of hard-core interactions and a spherically-symmetric square well attraction. The range of the attractive square well was fixed to $\Delta = 1.14 \sigma$, with σ the edge length of the cubes, and we varied the well-depth $\beta\epsilon$ with $\beta = 1/k_bT$. Unlike in the simulations presented in Figure 5 of the main text, we fixed all nanocube orientations to be parallel for improved simulation efficiency, and did not allow any rotation of the nanocubes over the course of the simulation. Note that this is not expected to affect the nucleation product significantly.

In Figure S12, we show one typical example of a nucleated supercrystal, for an overall packing fraction of $\phi = 0.015$ and an attraction strength of $\beta\epsilon = -4.4$. From snapshots like these we always observe the nanocubes to have nucleated into a ‘more or less’ cubic supraparticle.

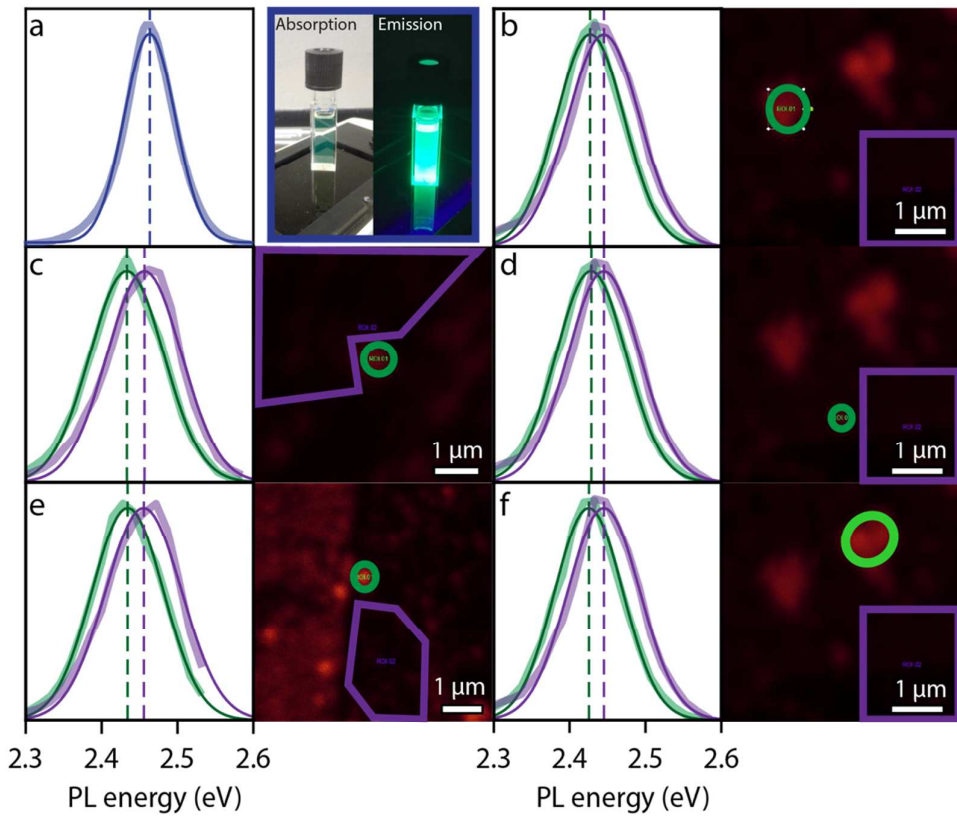


Figure S13: Additional confocal micrographs and PL spectra of single SPs. The data is shown as thick lines, whereas the Gaussian fits to the PL spectra are shown as thin solid lines. **(a)** The PL of a diluted NC dispersion. The digital photograph on the right shows the dispersion under normal daylight illumination, and illuminated by a UV lamp. **(b-f)** Various confocal micrographs and corresponding PL spectra of SPs (green) compared to the NC monolayer background (purple). In all measured spectra, we observe a consistent redshift of ~30 meV of the PL of the SPs compared to the NC monolayer background. The area in the micrograph indicates where we integrated the PL signal to obtain the displayed spectra.

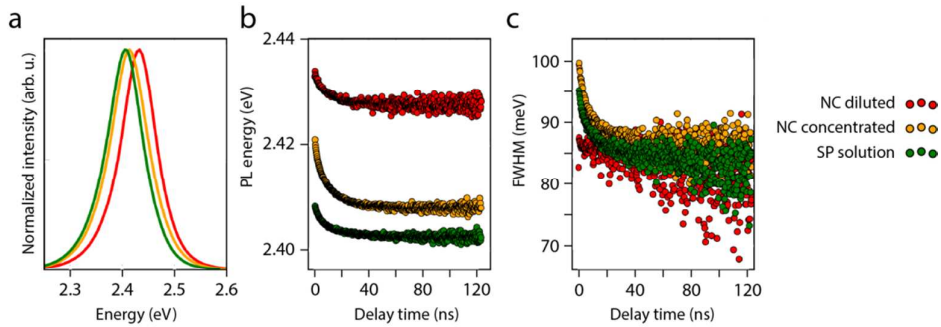


Figure S14: Time resolved emission spectroscopy (TRES) on NC and SP dispersions.

We compare solutions of NCs with two concentrations to solutions containing SPs. The concentrated NC dispersion has a concentration of $1 \mu\text{M}$ CsPbBr_3 NCs, whereas the diluted NC solution had a concentration of $10^{-3} \mu\text{M}$ CsPbBr_3 NCs. **(a)** Steady-state emission spectra of the diluted NC solution (red), concentrated NC solution (yellow) and SP solution (green). **(b)** Time evolution of the PL peak position over the first 120 ns. In all cases a redshift is observed. Research by De Weerd et al. has shown that there is the occurrence of non-radiative energy transfer between the NCs in solution through dipolar coupling or Förster Resonance Energy Transfer (FRET)⁸. We also observe a red-shift of the PL peak comparing the diluted and concentrated NC solutions. The observed redshift is increased in the SP solution. **(c)** Time evolution of the FWHM of the PL peak over the first 120 ns.

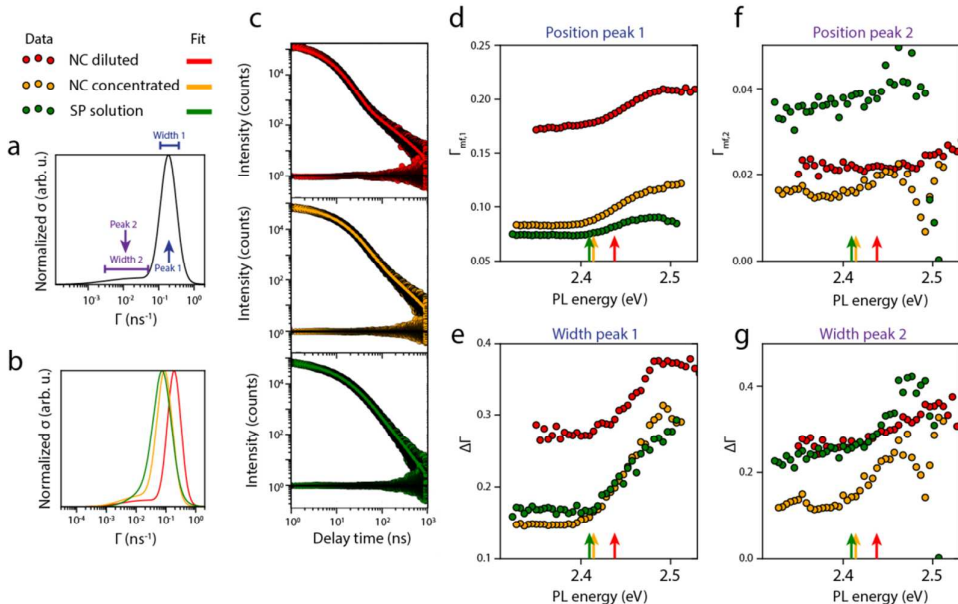
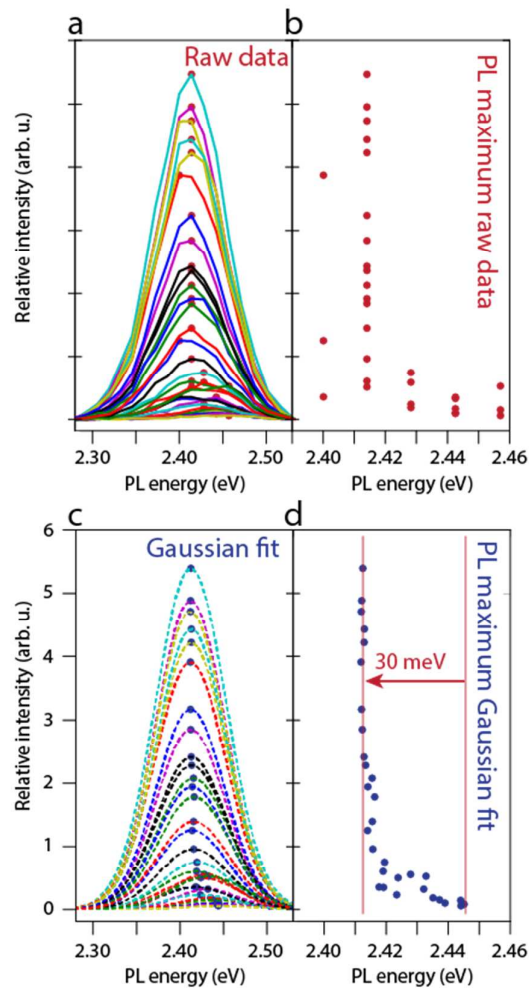


Figure S15: Time resolved emission spectroscopy (TRES) on NC and SP dispersions.

Detailed analysis of the time-resolved data. **(a)** We fit the data with the sum of two log-normal distributions⁹. The fitting procedure gives information on the distribution (or width, $\Delta\Gamma$) of two decay rates Γ . **(b)** Acquired decay rate distributions from the fits of the diluted NC dispersion (red), concentrated NC dispersion (yellow) and SP dispersion (green) as shown in **(c)**.

Analysis of the fast (**d**) and slower (**f**) decay rate components for the various PL energies and



their widths (displayed in (e) and (g)) respectively.

Figure S16: Comparison of the confocal microspectroscopy raw data and their Gaussian fits. (a) Raw PL data and the detected maximum of the peak profile. (b) Trend of intensity vs. PL energy for the raw data. (c,d) Same, but for the fitted Gaussian functions. The raw data and Gaussian fits show the same trend, i.e. the SPs emit 30 meV redshifted compared to the NC monolayer.

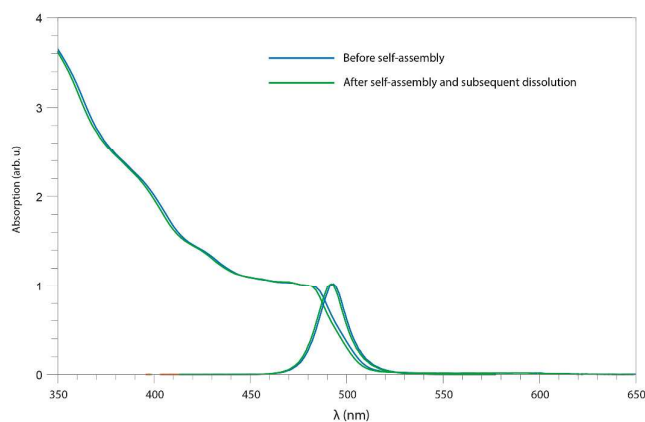


Figure S17: Comparison of the absorption and emission spectra before self-assembly of the nanocrystals and after dissolution of the supraparticles. A slight blueshift is observed, both in the emission and absorption spectrum after the self-assembly process, which might be due to some etching of the nanocrystals.

REFERENCES

- (1) De Roo, J.; Ibáñez, M.; Geiregat, P.; Nedelcu, G.; Walravens, W.; Maes, J.; Martins, J. C.; Van Driessche, I.; Kovalenko, M. V.; Hens, Z. Highly Dynamic Ligand Binding and Light Absorption Coefficient of Cesium Lead Bromide Perovskite Nanocrystals. *ACS Nano* **2016**, *10*, 2071–2081.
- (2) Hawkes, P. W. The Electron Microscope as a Structure Projector. In *Electron Tomography*; Springer US: Boston, MA, 1992; pp. 17–38.
- (3) Gilbert, P. Iterative Methods for the Three-Dimensional Reconstruction of an Object from Projections. *J. Theor. Biol.* **1972**, *36*, 105–117.
- (4) Guizar-Sicairos, M.; Thurman, S. T.; Fienup, J. R. Efficient Subpixel Image Registration Algorithms. *Opt. Lett.* **2008**, *33*, 156.
- (5) Penczek, P.; Marko, M.; Buttle, K.; Frank, J. Double-Tilt Electron Tomography. *Ultramicroscopy* **1995**, *60*, 393–410.
- (6) Mastronarde, D. N. Dual-Axis Tomography: An Approach with Alignment Methods That Preserve Resolution. *J. Struct. Biol.* **1997**, *120*, 343–352.
- (7) Otsu, N. A Threshold Selection Method from Gray-Level Histograms. *IEEE Trans. Syst. Man. Cybern.* **1979**, *9*, 62–66.
- (8) de Weerd, C.; Gomez, L.; Zhang, H.; Buma, W. J.; Nedelcu, G.; Kovalenko, M. V.; Gregorkiewicz, T. Energy Transfer between Inorganic Perovskite Nanocrystals. *J. Phys. Chem. C* **2016**, *120*, 13310–13315.
- (9) van Driel, A. F.; Nikolaev, I. S.; Vergeer, P.; Lodahl, P.; Vanmaekelbergh, D.; Vos, W. L. Statistical Analysis of Time-Resolved Emission from Ensembles of Semiconductor Quantum Dots: Interpretation of Exponential Decay Models. *Phys. Rev. B* **2007**, *75*, 35329.